REVIEW

National Science Review
5: 559–576, 2018
doi: 10.1093/nsr/nwx100
Advance access publication 29 August 2017

MATERIALS SCIENCE

Inorganic–organic halide perovskites for new photovoltaic technology

Dongmei Li[1,2], Jiangjian Shi[1,2], Yuzhuan Xu[1,2], Yanhong Luo[1,2], Huijue Wu[1] and Qingbo Meng[1,2,*]

ABSTRACT

Perovskite solar cells (PSCs) have received worldwide attention due to excellent power-to-electricity conversion efficiency (PCE). Currently, a PCE record of as high as 22.1% has been achieved, comparative to those of copper indium gallium selenide and CdTe solar cells. However, there are still some critical issues to solve, especially the stability issue at the current state, in order to promote PSC commercialization. In this respect, various device architectures and the working principle are briefly introduced. Then, key features of inorganic–organic hybrid perovskites and related film deposition methods are discussed. Typically, experimental and theoretical efforts to reveal the physical issues of the device are emphasized as well as the cell stability. Finally, a short summary, challenge and prospect are given.

Keywords: inorganic–organic hybrid perovskite materials, perovskite solar cells, heterojunction, photophysics, stability

[1]Key Laboratory for Renewable Energy (CAS), Beijing Key Laboratory for New Energy Materials and Devices, Beijing National Laboratory for Condensed Matter Physics, Institute of Physics, Chinese Academy of Sciences, Beijing 100190, China and [2]School of Physical Sciences, University of Chinese Academy of Sciences, Beijing 100049, China

*Corresponding author. E-mail: qbmeng@iphy.ac.cn

Received 29 April 2017; **Revised** 15 July 2017; **Accepted** 24 July 2017

INTRODUCTION

Thin-film solar cells are a promising type of cost-competitive solar power via cost-effective materials and fabrication technology, comparable with commercial silicon-based photovoltaics [1]. The bandgaps of CdTe (1.45 eV) and copper indium gallium selenide (CIGS, 1.04–1.68 eV) semiconductors can well meet the spectrum of sunlight, guaranteeing a power-to-electricity conversion efficiency (PCE) of over 22% for CdTe and CIGS thin-film solar cells; however, vacuum deposition and/or high-temperature processes are still needed [2–3]. Solution-processed technology represents the lowest-cost production method for thin-film solar cells, including spin-coating, blade-coating, spraying, inkjet printing, gravure printing, slot-dye coating and so on [4–5]. Recently, solution-processed perovskite solar cells (PSCs) have attracted worldwide attention due to their extremely high efficiency exceeding 22%, comparative to those of CIGS and CdTe solar cells and far exceeding dye-sensitized solar cells (DSCs) and organic photovoltaics (OPVs) [6]. It is very likely that a PCE of 25% may be achieved in the future [7]. Surprisingly, this progress has been achieved in only a few years along with rapid development of different device architectures, processing techniques and novel materials.

The excellent cell performance of PSCs mainly benefits from inorganic–organic hybrid perovskite materials with advantages of ease of fabrication, panchromatic sunlight absorption, high carrier mobility, superior carrier diffusion length, long carrier lifetimes and so on [8]. The first PSC based on $CH_3NH_3PbX_3$ (X = Cl and Br) as sensitizers was reported by Kojima *et al.* in 2009, exhibiting 3.8% PCE, which was further improved to 6.54% by Im *et al.* in 2011; however, a rapid degradation of the cell performance perplexed scientists [9–10]. The breakthrough came in 2012 when Kim *et al.* fabricated all solid-state mesoscopic heterojunction PSCs by using *spiro*-OMeTAD, presenting 9.7% PCE and relatively good stability [11]. Since then, some milestones in PCEs have emerged successively, which further stimulated the development of PSCs. In 2012, Lee *et al.* fabricated a 'meso-superstructured' PSC with 10.9% PCE by replacing the mesoporous TiO_2 with Al_2O_3 [12]. The successful application of this meso-structured insulating scaffold

demonstrated that the $CH_3NH_3PbI_{3-x}Cl_x$ perovskite material is extraordinarily effective, and can transport both electrons and holes between cell terminals and function well in a simplified device architecture even without scaffolds. In 2013, Burschka *et al.* reported a sequential two-step dipping method to fabricate PSCs with 15% and a certified 14.14% PCEs [13]. Subsequently, by the aid of compositional engineering and the 'anti-solvent one step deposition method', Saliba and Shin's groups independently achieved over 21% PCE [14–15]. In the meantime, the stability of the PSCs was improved by introducing Cs^+ and Rb^+ cations, adopting 2D perovskite films or using La–$BaSnO_3$ to replace conventional TiO_2 [15–17]. In addition, a certified 19.7% PCE for PSCs with an aperture area exceeding 1 cm^2 was also obtained [18].

Although the high efficiencies of PSCs have been frequently refreshed, the perovskite layers are subject to compositional degradation under high humidity and thermal treatment. Recent investigation reveals that the PSC may suffer from a change in the semiconductor electric properties while the cell operates. Therefore, long-term stability becomes a primary concern of the community [19]. On one hand, thermal stability is particularly important for solar cell operation; on the other hand, solar modules have to operate continuously between temperatures of −40 and 85°C as well as high solar irradiance over a long period of time [14].

In this review, we will briefly introduce the device architectures and the working principle. The key features of perovskite materials and film deposition techniques will also be reviewed. Typically, experimental and theoretical efforts to reveal the physical issues of the device are emphasized as well as cell stability. Finally, a short conclusion and prospect will be given.

DEVICE ARCHITECTURES

The huge success of PSCs not only lies in their high efficiencies but also their diversity in device architectures, all of which are derived from the distinctive optoelectric properties of the perovskite materials. It is also found that the evolution of device structures is also accompanied by the development history of the devices. In this section, we will briefly introduce different PSC structures and the development history of the devices.

The first PSC employed a mesoporous TiO_2 layer as a scaffold, which supported hybrid perovskite materials as sensitizers and transported photo-generated electrons [9]. Due to the fine carrier transportation ability of inorganic–organic hybrid perovskites, the device architecture has evolved and different PSC structures have emerged [20]. Mesoscopic structure employs a semiconductor oxide scaffold, which is fully infiltrated with the perovskite and can extend over the nanostructure to form a capping layer, so-called 'mesoporous structure', see Fig. 1a. A specific mesoporous PSC structure worth mentioning is based on a mesoporous Al_2O_3 insulating scaffold [12]. PSCs can also be fabricated without a mesoporous scaffold, so-called 'planar PSCs' [21]. Considering the position of the electron- or hole-transporting layer in front of the incident light, planar PSCs can be classified into *n-i-p* and *p-i-n* (inverted) structures; see Fig. 1b. Regardless of the light irradiation direction, the PSC generally consists of a conductive substrate (fluorine-doped tin oxide (FTO), indium-tin-oxide (ITO) or flexible ITO-polyethylene terephthalate (PET)), an electron-transporting layer (ETL), a perovskite layer, a hole-transporting layer (HTL) and a back electrode (Au or Ag). When PSCs are defined by whether they use an HTL or not, the HTL-free PSC is also an important branch; the HTL-free full-printable PSCs in particular exhibit good stability [22]. At present, mesoscopic systems exhibit a certified PCE of 22.1% on the National Renewable Energy Laboratory's best efficiency chart, slightly superior to planar embodiments with a PCE of 20.8% [6,23].

PSCs have been proved to be a free carrier-based device, in which the charge separation and transportation processes are more like a heterojunction solar cell [24–25]. To achieve efficient PSCs, the energy levels of these different components need to be well matched (see Fig. 1c, d). In addition, the key materials, fabrication techniques and interface engineering have to be optimized. In the meantime, a better understanding the dynamic processes of the device is also needed. Detailed discussion will be presented in the following sections.

PEROVSKITE MATERIALS AND FILM FABRICATION TECHNIQUES

Generally, optoelectrical materials with different chemical compositions exhibit different trends in their application. The hybrid organic–inorganic perovskite structures closely bridge organic and inorganic materials through a well-defined molecular assembly. In this section, we will review the basic properties of perovskite materials and the recent efforts in understanding the relationship between the composition, properties and fabrication techniques.

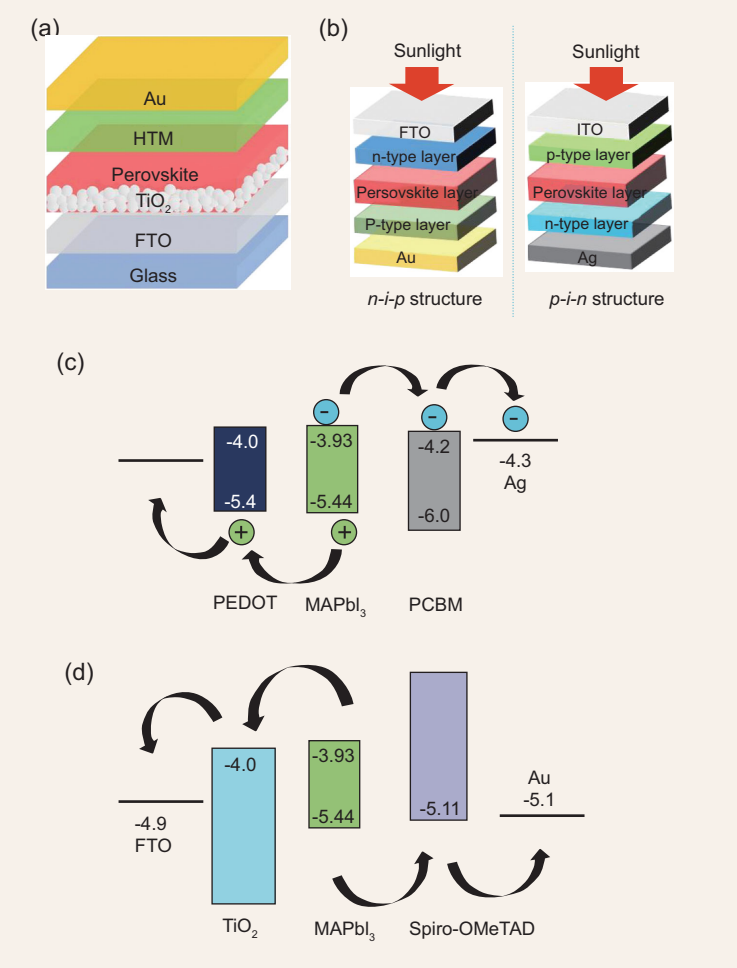

Figure 1. Schemes of basic PSC structures: (a) mesoporous PSCs; (b) planar PSCs with *n-i-p* and *p-i-n* cell architectures; (c) and (d) energy-level diagrams (eV) of routine PSC materials.

Engineering perovskite materials as light absorbers

Brief introduction to perovskites

The perovskite structure was first recognized as mineral calcium titanate ($CaTiO_3$). Halide perovskite, as a new branch of perovskite materials, exhibits attractive photovoltaic characteristics [26]. So far, all inorganic $CsBX_3$ (B = Sn, Pb; X = Cl, Br, I) and inorganic–organic hybrid perovskites have been successfully used in photovoltaic devices. Stoichiometric inorganic–organic hybrid perovskites, ABX_3 (A = organic cation, widely used methylammonium (MA) or formamidinium (FA); B = Pb, Sn; X = Cl, Br and I), are generally used to describe this kind of perovskite, which has a 3D structure with corner-sharing anionic BX_6 octahedra with the X atoms located in the corners and the B atom in the middle of the octahedra, and A cations located at interstices surrounded by eight octahedra in the cuboctahedral gap; see Fig. 2a. These hybrid perovskite materials present fascinating characteristics for high-performance photovoltaic devices, i.e. adjustable bandgap (optimal 1.4– 1.5 eV), high absorption coefficient (10^4–10^5 cm^{-1}), low exciton binding energy (<50 meV), ambipolar charge transport capability and long carrier diffusion length (~175 μm) [8,27,28]. In addition, relatively good crystallization and easy film formation derived from a solution-processed method at low temperature make them highly competitive, promising low-cost photovoltaic materials.

Generally speaking, the crystallographic stability and possible structure of perovskite ABX_3, even selecting A, B and X ions, have to consider an octahedral factor μ and a tolerance factor t:

$$\mu = \frac{R_B}{R_X} \quad (1)$$

$$t = \frac{R_A + R_X}{\sqrt{2}\,(R_B + R_X)} \quad (2)$$

where R_A, R_B and R_X represent the ionic radii of A, B and X ions. If t is in the range of 0.89–1.0, the perovskite material usually adopts a cubic structure, as shown in Fig. 2c; however, a lower t value will result in less symmetrical tetragonal or orthorhombic structures. When t is close to unity, the ideal cubic perovskite structure can be obtained. Calculated t and μ factors for a range of halide perovskites are shown in Fig. 2c [26]. Despite these constraints, transitions between such structures while heating are common for any given halide perovskites, such as $MAPbI_3$ (Fig. 3a) and $FAPbI_3$ (Fig. 3b), and the high-temperature phase is generally cubic [29]. In fact, a cation is generally considered to be the charge compensation in the lattice, and does not contribute to the band structure. However, variation of the A cation's size will strongly influence the optical property due to its deformation of the MX_6^{4-} octahedral network. Namely, smaller A cations (i.e. MA or FA) can maintain a 3D structure, whereas larger A cations (long chain alkyl or aryl ammonium) will result in lower-dimensional layered or confined perovskites, as seen in Fig. 2b.

The 3D halide perovskites have a high extinction coefficient (α) up to 10^5 cm^{-1} [30–31]. For example, the light absorption capability of $MAPbI_3$ is even higher than that of GaAs, which contributes to the best-performing single-junction solar cell, and two orders higher than that of crystal silicon [6]. According to the first-principles calculation, the electronic structure of $MAPbI_3$ is dominated by characteristics of the Pb–I bond, the valence-band maximum of which is characterized as an anti-bonding hybrid

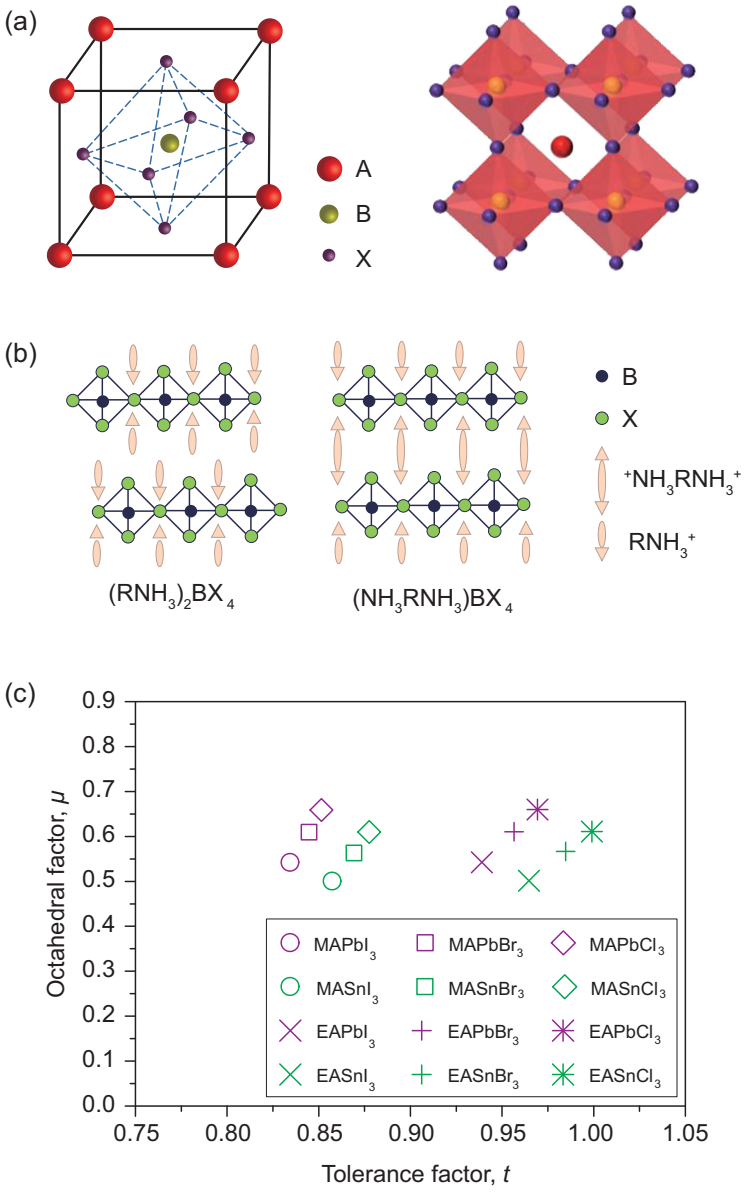

Figure 2. (a) The basic perovskite structure ABX_3 and their extended network structure connected by the corner-shared octahedral; (b) basic structures of 2D organic–inorganic perovskite with bilayer intercalated organic molecules; (c) calculated t and μ factors for 12 halide perovskites; EA represents $CH_3CH_2NH_3$ (Note: redrawn figure). Adapted with permission from [26].

state of Pb 6*s* and I 5*p* orbitals, while the conduction band minimum is characterized as a non-bonding hybrid state of Pb 6*p* and I 5*p* orbitals [32]. The high α is attributed to the high density of states in the conduction band minimum (CBM) of the perovskite, and direct *p*–*p* transition may be the origin. Due to the high α and strongly reflective back electrode, a 500-nm-thick perovskite film is enough to capture most incident photons with energies lower than the energy gap (E_g).

Perovskite film fabrication techniques

The morphology and crystallization of perovskite films will strongly influence the cell performance. In the meantime, high-quality perovskite film is susceptible to film deposition conditions and techniques. For the moment, three main film deposition methods are usually adopted: one-step precursor solution deposition, two-step sequential deposition (including the vapor-assisted solution process) and vapor deposition, as shown in Fig. 4.

One-step precursor solution deposition

At the initial development stage of PSCs, the one-step precursor solution deposition method was used most often; it was carried out by directly spin-coating the mixed solution on the substrate, and the precursor solution was obtained by dissolving all the precursor salts in high-boiling-point polar solvent (i.e. dimethylformamide (DMF), dimethylsulfoxide (DMSO), γ-butyrolactone (GBL)), as shown in Fig. 4a [11]. Aiming at uncovered pinhole areas derived from large $MAPbI_3$ grains, Zhao *et al.* developed a one-step, solvent-induced, fast crystallization method (the so-called 'anti-solvent method') involving spin-coating a DMF solution of $MAPbI_3$ followed immediately by exposure to chlorobenzene to induce perovskite crystallization for planar PSCs [33]. So far, by using the anti-solvent method combined with compositional engineering, over 21% PCE has been achieved [14–17,34]. In addition, a simple alternative vacuum flash-assisted deposition method was reported by Li *et al.*, which enabled a certified record PCE of 19.6% for a 1-cm^2-sized device and a maximum efficiency of 20.5% without hysteresis [35]. Overall, the anti-solvent one-step method can clearly induce rapid nucleation and slow crystal growth processes during the perovskite film formation, thus providing an effective way to achieve high-quality perovskite crystals. In the meantime, this method is suitable for all PSC structures (planar vs. mesoporous), and it may be one possible way to realize the large-area manufacturing.

Two-step deposition method

A sequential two-step dipping technique was first reported by Mitzi in 1998, then Burschka *et al.* in 2013 [13]. In a typical two-step method, PbI_2 is firstly spin-coated onto the substrate, followed by exposure to the organic ions either in solution or in vapor to afford the perovskite film (Fig. 4b). This method presented the first 15% PCE with a certified 14.14% PCE [13]. Subsequently, aiming at solving incomplete conversion of PbI_2 and uncontrollable crystal size and surface morphology, different post-treatment methods have also been developed;

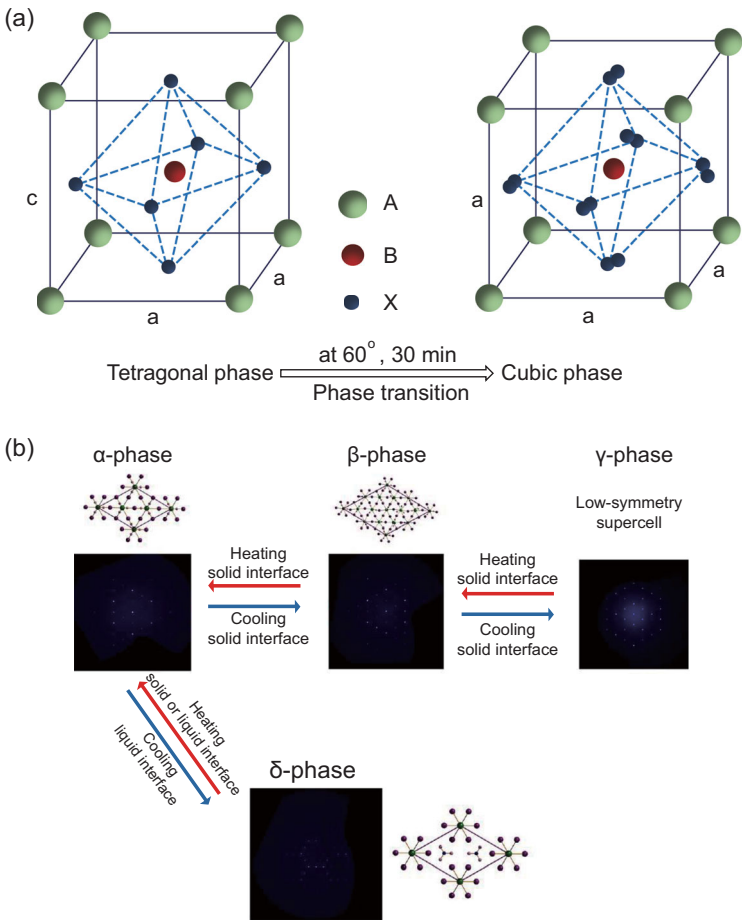

Figure 3. Graphical schemes of the structural transformation of (a) the $MAPbI_3$ perovskite and (b) the $FAPbI_3$ perovskite. Adapted with permission from [29].

e.g., Zhu *et al.* and Xiao *et al.* reported a pressure-assisted morphology reconstruction method and temperature-assisted sequential deposition method to control film morphology and interfacial charge transport property for high-efficiency PSCs, respectively [36–37].

The vapor-assisted solution process (VASP) can be considered as another kind of two-step method, as shown in Fig. 4b [38]. This method is different from the conventional two-step solution process and vacuum deposition, and takes advantage of the kinetic reactivity of methylamine iodide (MAI) and the thermodynamic stability of perovskites during the film growth process and affords well-defined grain structures with sizes up to micron-scale, full surface coverage and smooth surface without pinholes. Currently, various VASP film growth techniques have been developed, such as hybrid chemical vapor deposition (HCVD), hybrid physical chemical vapor deposition (HPCVD), low-pressure chemical vapor deposition (LPCVD), *in situ* tubular chemical vapor deposition (ITCVD) and modified chemical vapor transport (mCVT) [39]. 18.9% PCE was obtained under ambient atmosphere by a modified VASP method [40]. VASP presents a simple, controllable and versatile method for high-quality perovskite films and high-efficiency PV devices.

Vapor deposition method

Vapor deposition techniques are widely used in the semiconductor industry for largescale production in optoelectronic applications. Perovskite films derived from the vapor deposition process under vacuum were first reported by Salau *et al.* [41], then by Mitzi *et al.* [42]. In 2013, Liu *et al.* modified this technique as a dual-source vapor deposition method for pinhole-free $MAPbI_{1-x}Cl_x$ perovskite films with hundreds of nanometer-scale crystals for planar PSCs; see Fig. 4c [43]. Malinkiewicz *et al.* fabricated an inverted *p-i-n* planar PSC with sublimated $MAPbI_3$ perovskite layer [44]. Recently, the chemical vapor deposition (CVD) method was also reported by precisely controlling the crystallization process [45]. Vapor deposition techniques are suitable for multilayered thin-film structures and a variety of substrates; however, this technique demands high vacuum.

Compositional engineering

As we know, tailoring the bandgap of the light absorber is important for minimizing the energy loss and improving the cell performance. A material engineering in terms of AMX_3 compositional control is necessary; namely, the absorption range and the E_g value of these perovskites can be adjusted by ion substitutions [28,47]. In addition, the E_g value of a semiconductor is related to the lattice size and the atomic interaction according to the tight-binding approximation theory. $MAPbI_3$ can absorb the widest range of visible light, showing an E_g value of about 1.5 eV; however, the E_g value of $MAPbBr_3$ is about 2.3 eV. Noh *et al.* reported $(MAPbI_3)_{1-x}(MAPbBr_3)_x$ mixed perovskite by material engineering, the bandgap (E_g) of which can be changed from 1.57 to 2.29 eV by the following equation $E_g(x) = 1.57 + 0.039\,x + 0.33\,x^2$. This mixed perovskite with $x \geq 0.2$ exhibits higher stability toward the humidity than those with $x < 0.2$ [48]. In the chlorine substitution of $MAPbI_3$, the main role of the chloride is not to regulate the bandgap. Instead, the introduction of chloride into $MAPbI_3$ mainly improves the film morphology, preferential orientation, crystallinity, grain size and so on, which can further improve carrier transport across the heterojunction interface, passivate the grain boundary and result in higher cell performance [49]. Partial replacement of halides with the pseudohalide SCN^-, $MAPbI_{3-x}(SCN)_x$, has also been reported; this

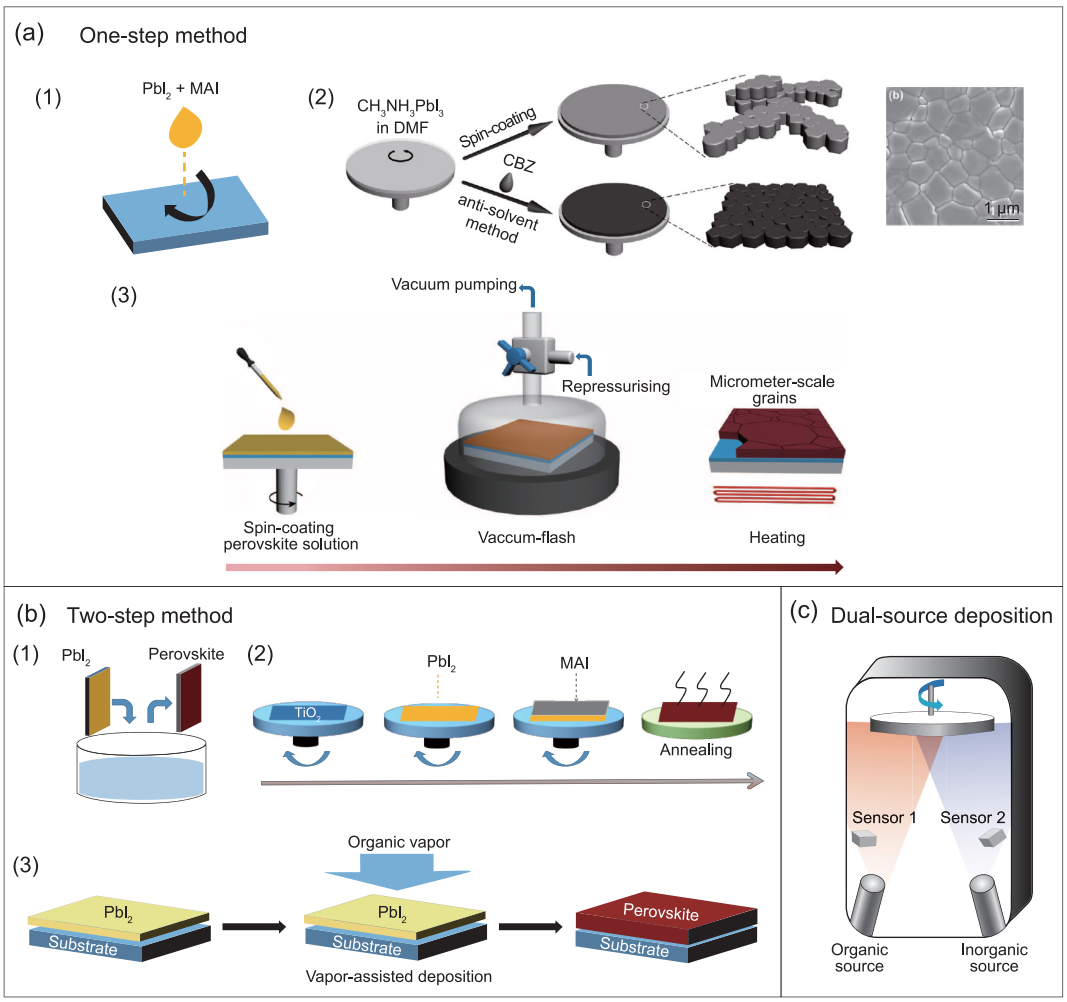

Figure 4. Three general perovskite film fabrication methods: (a) one-step precursor deposition method (CBZ: chlorobenzene); (b) sequential deposition method; (c) dual-source vapor deposition method. Adapted with permission from [33,35,43].

exhibited good humidity-resistance characteristics, thus leading to enhanced moisture stability of the PSCs [50–51]. In fact, based on the investigation of single crystals grown under the same conditions, 2D structured $(MA)_2Pb(SCN)_2I_2$ is suggested instead [52]. Xiao *et al.* further investigated this 2D $(MA)_2Pb(SCN)_2I_2$ by the aid of experimental measurement and DFT calculation, and found that its bandgap is about 2.0 eV, larger than that of $MAPbI_3$; in the meantime, the carriers are confined within the 2D layers [53]. PCEs of 8.3% were reported for mixed $(MA)_2Pb(SCN)_2I_2/MAPbI_3$ devices [54].

When larger-sized FA $(HC(NH_2)_2^+)$ occupies the A site of the perovskite lattice, the E_g value can be reduced to about 1.47 eV, closer to the desired E_g of 1.4 eV. In addition, $FAPbI_3$ has other advantages over $MAPbI_3$, such as a smaller polarization dipole, stronger *p*-type characteristics and higher thermal stability. For $FAPbI_3$-based PSCs, a higher photocurrent can be obtained but with a lower photovoltage, and a non-perovskite phase is found to restrict the cell performance [55]. Therefore, the E_g needs to be optimized for a balance. $(FAPbI_3)_{0.85}(MAPbBr_3)_{0.15}$ mixed perovskite derived from $FAPbI_3$, $FAPbBr_3$, $MAPbI_3$ and $MAPbBr_3$ can afford a complete perovskite phase, in which the PCE was increased to 20.8% with a negligible hysteresis [15]. Very recently, PSCs based on triple and quadruple cation perovskites $(CsRbMAFAPb(I/Br)_3)$ have been fabricated; which exhibited a PCE of 21.6% with an average PCE of 20.2% and stabilized 19.0% on a 0.5 cm^2 cell. In addition, polymer-coated cells can maintain 95% of their initial performance at 85°C after 500 aging hours under full illumination and maximum power point tracking [14,16]. Obviously, compositional engineering is feasible to fabricate highly efficient PSCs with better stability and reproducibility.

Replacing the metal cation is another method of narrowing the bandgap; in the meantime, developing lead-free perovskite photovoltaics is also in line with the environmental regulations. Jain *et al.* used high-throughput density functional theory calculations to screen lead-free perovskite-like materials and found that about 10 compounds (A = Na, K, Rb, Cs, Cu and Ag; B = Ga, In and Sb; X = Cl, Br and I) have bandgaps in the range of 1.5–2.5 eV and exhibit potential application in lead-free photovoltaic devices [56]. Pure Sn halide perovskite itself only exhibited a PCE of over 6% and poor stability [57–58]. However, according to the first-principles calculation, when Pb atoms are partially substituted by Sn atoms, the E_g decreases instead, probably due to weaker atomic interactions between Sn and halides [59]. E_g can be further reduced to 1.16 eV when mixed Sn/Pb atoms occupy the B site, and a steady decrease in E_g is also verified by theoretical calculation and experimental measurement [60]. Although a higher photocurrent could be obtained by decreasing the E_g with Sn substitution, a much lower device performance was presented instead due to high hole doping or defects, and the existence of Sn atoms also resulted in low stability [57]. Bismuth (Bi^{3+}) can be used as a nontoxic replacement for Pb-based perovskite due to its similar electronic structure to Pb^{2+}. Recently, some efforts have been made to incorporate Bi^{3+} as the B-site cation in the ABX_3 perovskite framework. $(MA)_3Bi_2I_9$ perovskite possesses a bandgap of 2.1 eV and cannot realize the high cell performance; however, the bandgap was significantly reduced to 1.45 eV after sulfur doping, which was supposed to be more suitable for application in photovoltaics [61]. Some work reported that, in the formation of 2D Bi^{3+}-halide perovskites, Bi^{3+} has been incorporated into the lattice with vacancy formation on the B site and an organic cation as the template [62]. Slavney *et al.* reported a double-perovskite structure $Cs_2AgBiBr_6$ with an indirect bandgap of 1.95 eV, suitable for a tandem solar cell [63].

So far, compositional engineering with A and X site substitutions has brought about tremendous success. For a single-crystal $MAPbI_3$ perovskite, the absorption edge is red-shifted with E_g lower than 1.5 eV. This may be due to the difference in lattice size and defect properties between the surface and the bulk of perovskite crystals [64]. Currently, the cell performance based on single-crystal perovskites is still unsatisfactory.

Crystal growth engineering

A high-quality perovskite film is the key to high-efficiency PSCs, and this kind of high-quality perovskite film refers to films with fewer defects and trap states derived from pinholes, crystal defects and grain boundaries. As we know, inorganic–organic halide perovskite films can be easily obtained in mild conditions due to a low lattice energy. Therefore, whatever fabrication method is adopted, it is necessary to effectively control the perovskite growth process. In fact, when the perovskite formation rate is high, it is hard to control crystal growth. The Lewis acid–base adduct method has been recognized as a viable way to regulate perovskite crystal growth. A Lewis acid is defined as an electron-pair acceptor and a base as an electron-pair donor. The Lewis acid–base reaction will lead to either a redox reaction or adduct formation, and adducts are generally a kind of coordination compounds. For inorganic–organic halide perovskites, Pb(II) halides are typical Lewis acids, which can afford adducts with monodentate or bidentate ligands in 1: 1, 1: 2 or 2: 1. Monodentate or bidentate ligands (Lewis bases) usually contain O-donors (e.g. DMSO, *N*-methyl-2-pyrrolidone (NMP)), S-donors (e.g. thiourea, thioacetamide) and N-donors (e.g. pyridine).

Initially, this adduct-induced perovskite film growth method is supposed to strongly retard the rapid crystallization of PbI_2, which is based on the strong interaction between Pb^{2+} and S = O from DMSO. Jeon *et al.* first prepared the PbI_2(DMSO) precursor, which was further applied to fabricate the $FAPbI_3/MAPbBr_3$ by direct intramolecular exchange with FAI/MABr, presenting a PCE of 20.2%, as shown in Fig. 5 [46]. Then, the mixture of DMSO and DMF was directly adopted to give an adduct of $MAI{\cdot}PbI_2{\cdot}$DMSO, since PbI_2 prefers to coordinating with DMSO relative to DMF due to its stronger Lewis basicity [65]. This exchange does not induce volume expansion or change the film thickness due to the similar molecular volumes of DMSO and FAI, and the perovskite film is extremely uniform and flat as well. Recently, Jo *et al.* reported that a PbI_2(NMP) complex (NMP = *N*-methyl-2-pyrrolidone) as an intermediate can also convert into high-quality perovskites. Larger perovskite grain size was obtained from the PbI_2(NMP) film than from the PbI_2(DMSO), which can reduce bulk defects and improve charge carrier mobility, thus leading to a PCE of 19.5% [66–67]. When the $FAPbI_3$ film was fabricated by this adduct method, however, thiourea as an S-donor was preferred rather than DMSO as an O-donor due to its stronger coordination ability, and a 1:1:1 adduct of $FAI{\cdot}PbI_2{\cdot}$thiourea is suggested. The resulting $FAPbI_3$ films showed better cell performance because of faster charge transport and the reduced trap states [68]. In addition, this kind of Lewis acid–base

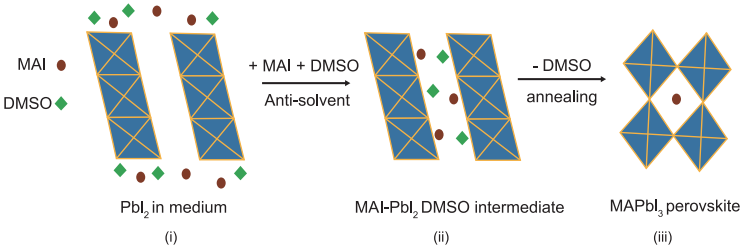

Figure 5. Scheme for perovskite formation via the MAI–PbI_2–DMSO intermediate: (i) PbI_2 with edge-sharing $[PbI_6]^{4-}$ octahedral layers; (ii) the formation of flat MAI–PbI_2–DMSO intermediate phase by MAI and DMSO molecules intercalated between the layers while toluene is introduced to the wet film with PbI_2, MAI and DMSO; (iii) conversion of MAI–PbI_2–DMSO into the perovskite phase with corner-sharing octahedra by removing DMSO molecules while annealing. Adapted with permission from [46].

intermediate adducts plays a crucial role in controlling the morphology of perovskites. Crystal growth engineering via Lewis acid–base adducts is expected to afford homogeneous films with large grain sizes since the removal of the Lewis base in the adduct can also reduce perovskite crystallization rate.

In order to improve the crystallization quality and reduce defect states of the perovskite films, some additives have also been introduced. Yang *et al.* introduced additional iodide ions into the organic cation solution, which was subsequently used for the intramolecular exchange process for perovskite films. Their distinctive work lies in the fact that their iodide solution was actually triiodide (I_3^-) solution, which was obtained by stirring iodine (I_2) in isopropanol (IPA) at 80°C and reducing some I_2 molecules to I_3^- ions. Further investigation revealed that I_3^- decreased deep-level traps in bulk perovskite layers, thus leading to a PCE as high as 22.1% with a certified PCE of 19.7% [69]. However, unlike Yang's work, Liu *et al.* used a small amount of methylamine solution as an additive to eliminate small I_2 and polyiodide colloids in the precursor solution, also leading to reduced defect density and extended carrier diffusion length in the resultant film [70]. Obviously, a thorough understanding a variety of defect states as well as the origin is desirable in the future.

PHYSICS IN PEROVSKITE SOLAR CELLS

Although a certified PCE of 22.1% is presented in the NREL best efficiency chart [6], some important issues still need to be clarified. In addition to the stability, the discrepancy in reverse and forward scanned current–voltage curves, so-called 'hysteresis', is also an obstacle. Therefore, deep understanding the physics involved in PSCs is essential for developing stable and highly efficient devices.

Doping, carrier and electric properties

Point defects and doping

Point defects and self-doping of a multiple-component semiconductor are permanent topics, especially in understanding the physical properties of a photovoltaic material. As a ternary semiconductor, organic halide lead hybrid perovskites can be stable in a certain thermodynamic region [71]. In this region, the composition of halide perovskite materials may deviate from stoichiometry more or less, forming point doping or defects, such as ion vacancies, interstitials and substitutions. The self-doping properties of the perovskite $MAPbI_3$ are shown in Fig. 6. Iodide interstitial (I_i), cation substitution (MA_{Pb}), cation vacancies (V_{MA} and V_{Pb}) and anti-substitutions (e.g. I_{MA} and I_{Pb}) will introduce shallow acceptor doping levels, while deep defects may be caused by the I_{MA} and I_{Pb}. On the other hand, the cation interstitial (MA_i and Pb_i), anion vacancies (V_I), cation substitution (Pb_{MA}) and anti-substitutions (e.g. MA_I and Pb_I) will introduce shallow donor doping levels, while Pb interstitial and anti-substitution will cause deep defects. Generally speaking, it is still dependent on their formation energies in the thermodynamic region whether these self-doping levels could appear while the perovskite film is growing. The formation energy is mainly related to growth conditions. For example, the Pb vacancy easily appears in the I-rich/Pb-poor condition instead of the I-poor/Pb-rich condition. In experiments, this self-doping may be influenced by the film deposition method, precursor compositions, thermal treatment temperature and crystallization process. Wang *et al.* found that the doping type of $MAPbI_3$ is strongly dependent on the molar ratio of PbI_2/MAI in the one-step deposition process, and more MAI would lead to *p*-type perovskite [73]. They also found that the interdiffusion method is beneficial to the growth of *p*-type $MAPbI_3$ film whereas the hole concentration will decrease while prolonging the annealing time. For the two-step method, the hole concentration could be adjusted by the MAI concentration, and higher hole concentration was obtained by using a more diluted MAI solution [74]. For Sn-based perovskites, the exotic self-doping ability of the Sn-based perovskites allows them to adopt electrical properties from semiconductor to metallic, which are dependent on the synthetic procedures [58,75]. In particular, easy oxidization of Sn^{2+} to Sn^{4+} will cause materials doped with Sn^{4+}, which behave as *p*-type semiconductors, however, displaying metal-like conductivity, e.g. the electron and hole mobilities of $MASnI_3$ are estimated to exceed 2000 and 300 $cm^2/(Vs)$, respectively [76].

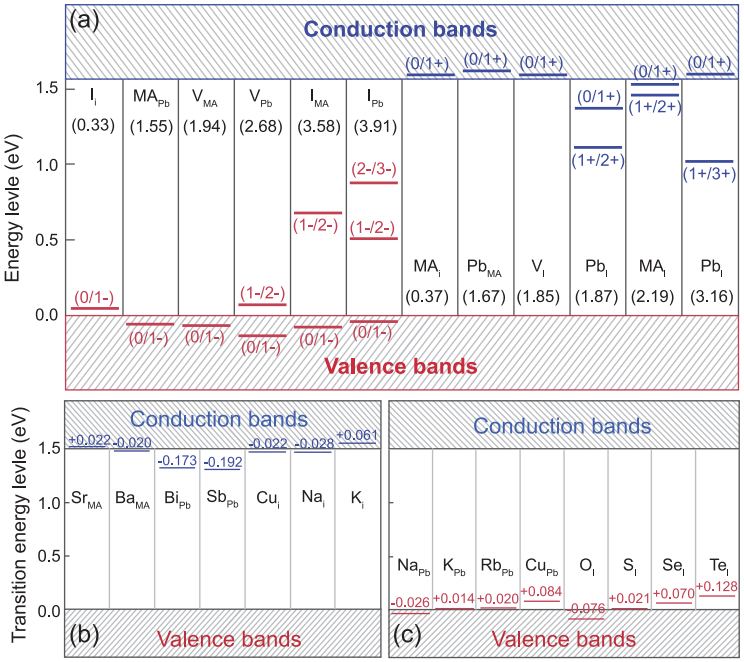

Figure 6. (a) Calculated transition energy levels of intrinsic point defects in $CH_3NH_3PbI_3$, and possible (b) donor and (c) acceptor doping by impurity atom substitution or interstitial. Adapted with permission from [71,72].

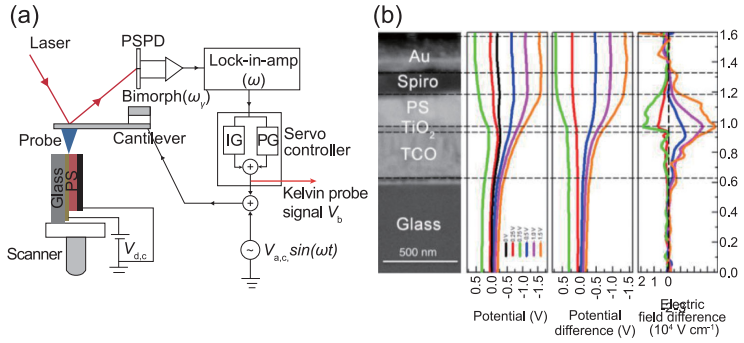

Figure 7. (a) Schematic diagram of the Kelvin probe force microscopy (KPFM) for the measurement of surface contact potential across the cell. (b) KPFM results and derived electric field properties of a planar perovskite solar cell under different steady-state bias voltages. Adapted with permission from [85].

Besides self-doping, *p*- or *n*-type doping by impurity atoms has also been theoretically studied [77]. Yan *et al.* found that cation substitutions with higher valent atoms or cation interstitials could give more free electrons to the perovskite system, so-called '*n* doping' [72]. On the other hand, ion substitutions with lower valent atoms would bring about electron-deficient energy levels, capturing the electrons in the valence band maximum (VBM) and causing *p* doping, as shown in Fig. 6c. Recently, the doping toward the Pb atom (such as Sb, In, Rb, Cu and Ag) has been reported to enhance the efficiency and stability of the solar cell [24,78–80]. However, little experimental work could directly confirm the doping and carrier properties.

Junction and electric field

According to the basic principles of semiconductor physics, a junction with a built-in electric field may form when two materials with different Fermi energy levels electrically contact with each other [81]. However, this concept was not widely accepted in the early developing stage of PSCs until more and more real-space nanoscale electric measurements were carried out [82].

Kelvin probe force microscopy (KPFM) is an effective approach to investigate the potential and electric field properties inside the cell [83]. By the aid of KPFM, a potential distribution is found in the perovskite and the TiO_2-based mesoscopic PSC, and a large electric field of about 10^6 V m^{-1} can be derived. A similar result was obtained in the planar cell with a ~300-nm-thick depletion region [84]. In these measurements, no obvious depletion was found in the *n*–TiO_2 layer. This agrees well with the junction theory since the majority electron concentration in the TiO_2 is much higher than the majority hole in the perovskite absorber.

To exclude the influence of surface defects for a more reliable result, steady-state bias voltages are applied at the cell to produce potential and electric field differences [85]. The KPFM setup for this measurement is depicted in Fig. 7a, where a voltage source is connected to the electrodes of the cell and the nanoscale potential across the cell is probed by the Kelvin probe. When a positive bias voltage is applied at the cell, the electric field strength in the perovskite absorber obviously decreases, in good agreement with the junction theory, as shown in Fig. 7b. Also, almost no electric field change can be observed in the TiO_2 and *spiro*-OMeTAD layers, which further confirms that the depletion region is mainly located in the perovskite region. However, if the perovskite absorber is thick enough, the depletion will also appear in the transparent conductive oxide layer. When a negative bias voltage is applied, more significant depletion can be observed. Less electric field change is observed in TiO_2 and *spiro*-OMeTAD layers, which further tells us that the bias voltage is mainly applied at the perovskite absorber due to its low carrier density and conductivity. Another important result is that no junction forms at the perovskite/*spiro*-OMeTAD interface although doped *spiro*-OMeTAD is usually a heavy *p*-type semiconductor. One reason for this is that the perovskite absorber usually has a hole density of about 10^{14}–10^{16} cm^{-3} [86–87]. Therefore, the Fermi energy level of the perovskite absorber is about −5.2 eV [88], much closer to the highest occupied molecular orbital (HOMO) energy level of the *spiro*-OMeTAD; thus, no obvious junction is found. Another possible reason lies in

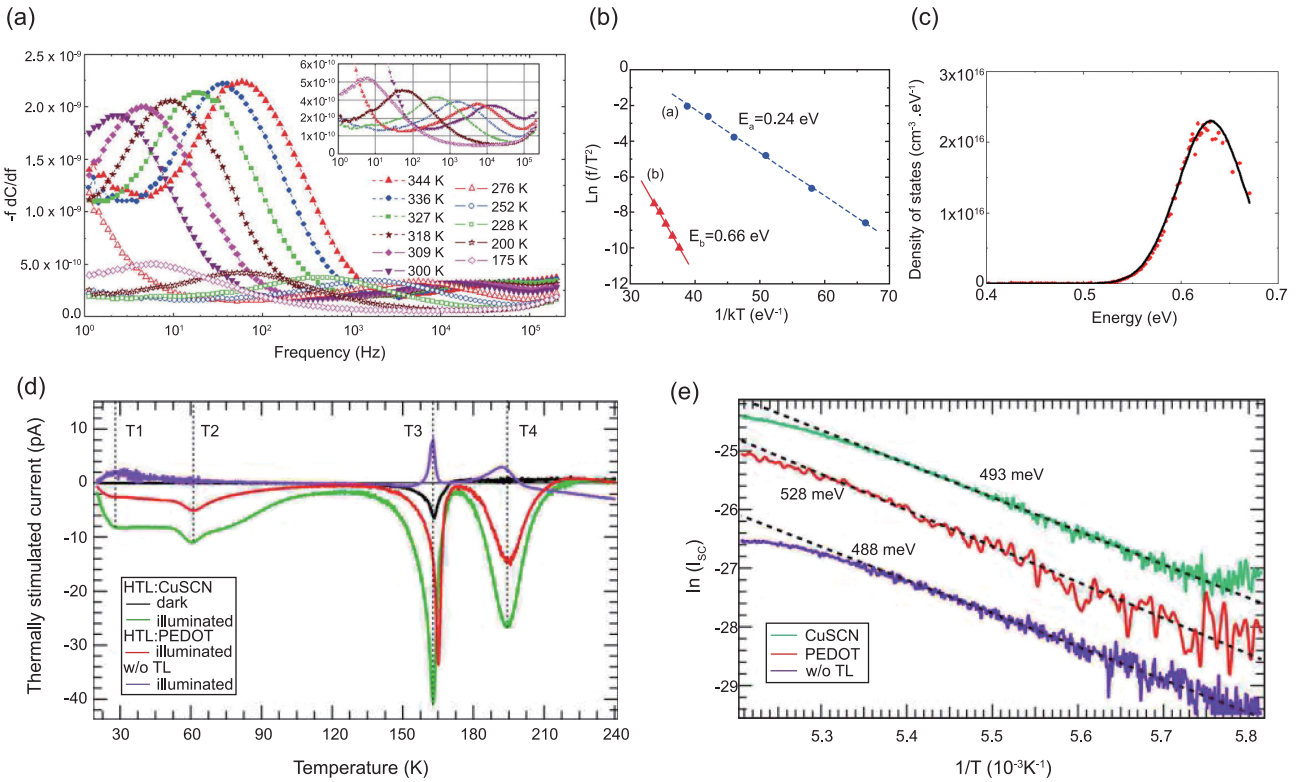

Figure 8. (a) Capacitance as a function of frequency of the PSC with a structure of ITO/PEDOT:PSS/$MAPbI_3$/PCBM/Al; (b) Arrhenius curves derived from the capacitance spectra, giving defect activation energies of 0.24 and 0.66 eV from the curves; (c) thermally stimulated current (TSC) spectra of PSCs with different device architectures; (d) and (e) defect activation energies derived from the TSC spectra. Adapted with permission from [89–90].

different charge transfer mechanisms between the organic charge transporting layer (CTL) and the inorganic semiconductor, which still needs more fundamental investigation.

Defect properties and relative measurement methods

Carrier property is not only determined by shallow doping; deep defects also have a significant influence on the charge dynamics and the performance of the semiconductor device. For example, deep defects can be caused by self-doping under certain film deposition conditions, as shown in Fig. 8a. Besides bulk defects, defects may also exist on the crystal surface and grain boundaries due to uncoordinated atoms and active electronic sites. In experiments, the low-temperature solution process is supposed to easily bring the impurity into the perovskite crystal, which may also cause deep defects. Some characterization methods have been applied to investigate deep defects in the perovskite material, especially in $MAPbI_3$. By replacing the oxygen atom on *spiro*-OMeTAD with a sulfur atom, which can effectively lower the highest occupied molecular orbital of the molecule, a stronger Pb–S interaction with perovskites occurs, thus leading to efficient hole extraction and surface trap passivation [91].

Thermal admittance (capacitance) spectroscopy (TAS) is an effective approach to obtain the defect distribution (i.e. defect density and activation energy) and dynamic information (i.e. capture velocity and escape frequency) in the absorber [92]. A complete device is needed in TAS measurement to ensure that the perturbation voltage can be applied at the absorber. According to the theory for admittance (capacitance) spectra, the distribution of defect density, $N_t(E_\omega)$, is obtained by the following equation:

$$N_t(E_\omega) = -\frac{V_D}{qW_D}\frac{\omega}{KT}\frac{dC}{d\omega}$$

where V_D and W_D are the heterojunction potential barrier and depletion width derived from the Mott–Schottky measurement, respectively; ω and C are the angular frequency and capacitance from capacitance spectra, respectively; K is the Boltzmann constant and T is the absolute temperature. E_ω, defined as the energy above the VBM, is obtained as follows:

$$E_\omega = KT\ln\frac{2\beta_p N_V}{\omega}$$

where β_p is the hole coefficient and N_V is the effective density of states in the valence band. To obtain

β_p and N_V, a temperature-dependent capacitance spectrogram is needed. The minimum E_ω value is the energy difference between the Fermi energy and the VBM, usually larger than zero. To accurately evaluate the defect distribution, capacitance spectra at different temperatures and Mott–Schottky curves are also needed. Figure 8a gives an example of capacitance spectra ($-f \times dC/df$) at different temperatures [89]. For each curve, a peak corresponds to a certain frequency, and the peaks appear at a lower frequency while at relatively high temperatures, or at higher frequency while at relatively low temperatures. The peak $-f \times dC/df$ at higher temperatures is much larger than that at lower temperatures, indicating that two defect energy levels with different densities may coexist in the bandgap. Arrhenius curves are thus derived with these feature frequencies in Fig. 8b. Clearly, two distinct curves exist at different temperature regions, the slopes of which tell us that the perovskite $MAPbI_3$ has two defect energy levels of 0.24 eV (E_a) and 0.66 eV (E_b) above the VBM. Heo *et al.* observed a defect energy level of about 0.28 eV, generally in agreement with E_a in Fig. 8b, and the density of states (DOS) is on the order of about 10^{17}– 10^{18} cm^{-3} eV^{-1} [93]. Huang and co-workers reported a defect energy level of ∼0.35 eV, and a much lower DOS of ∼10^{12} cm^{-3} eV^{-1} in the interdiffusion-deposited film [92,94]. The calculated defect density distribution is shown in Fig. 8c; the DOS of the defects centered at ∼0.62 eV is on the order of 10^{16} cm^{-3} eV^{-1}. Snaith and co-workers used a transient photoluminescence (PL) method to evaluate the defect density of the perovskite film of about 10^{16}–10^{17} cm^{-3} eV^{-1} [95–96]. Current–voltage measurements were used to estimate a defect density of about 10^{15}–10^{16} cm^{-3} (∼10^{16}–10^{17} cm^{-3} eV^{-1}) [97]. Importantly, the defect density can be significantly decreased by increasing the perovskite crystal quality [98].

Thermally stimulated current spectroscopy (TSC) is also an effective method to evaluate the defect distribution in a high-resistivity semiconductor, II-VI and III-V semiconductor materials [99–100]. By using this method, the current originating from the carriers released from trap defects is measured while increasing the sample temperature at a certain rate. Figure 8d shows the TSC spectra of $MAPbI_3$ perovskite devices with different structures. T_1 and T_2 TSC peaks at low temperature were assigned to shallow defects in the PCBM/C60 layers; however, the T_3 peak was due to the lattice phase transition of $MAPbI_3$. The T_4 peak was finally assigned to deep defects in the perovskite. Arrhenius curves for different device structures were finally derived in Fig. 8e. A deep defect energy level of about 508 ± 20 meV with a density of about 10^{15} cm^{-3} (∼10^{16} cm^{-3} eV^{-1}) was estimated and the trap density was basically consistent with that evaluated from the TAS method; however, the energy positions of the defect and the type (electron or hole) still need further clarification. However, where these defects are from, in bulk, film surface or grain boundaries, is still a question.

Ion migration and its influence on doping and defect

As discussed above, the carrier and defect properties of the perovskite film are related to the intrinsic doping, while the intrinsic doping is influenced by the localized element distribution inside the film. Recently, it has been found that the element distribution in the perovskite is significantly influenced by the external measurement conditions, such as bias voltage and illumination [101–103]. Ion migration is considered as the origin for element redistribution, which has been a hot research topic on the material and physics properties of the perovskite [104]. Xiao *et al.* first reported the ion migration and its influence on the photoelectric behaviors of the perovskite device [105]. Theoretical calculation based on DFT suggests the mechanism of ion migration, revealing that the ion migration activation energy is as low as about 0.5 eV [106]. In addition, the ions can easily migrate under an electric field of about 10^6 V/m, similar to the strength of the built-in electric field. Furthermore, the distribution of MA^+ cations in the perovskite film was observed by using spatially resolved photothermal induced resonance (PTIR) microscopy, and the MA^+ was found to migrate and accumulate at the perovskite/cathode interface, as shown in Fig. 9a. A distribution of electric potential was also observed in the film, possibly due to a *p–n* homojunction derived from the ion accumulation induced doping, see Fig. 9b. This implies that the ion migration under electric field will change the localized carriers and electrical properties of the film.

More importantly, ion migration is supposed to be an origin of the anomalous photoelectric hysteresis in PSCs. Xiao *et al.* suggested that the doping effect caused by the ion migration is the physics mechanism of the hysteresis. The doping and the homojunction formation may change the net charge distribution inside the film. On the other hand, based on theoretical calculation, Reenen *et al.* investigated the interfacial charge accumulation is due to ion migration [107]. They suggested that charge accumulation alone would not lead to the hysteresis and the traps at the interface also have to be considered, as shown in Fig. 9c. A steady-state bias voltage

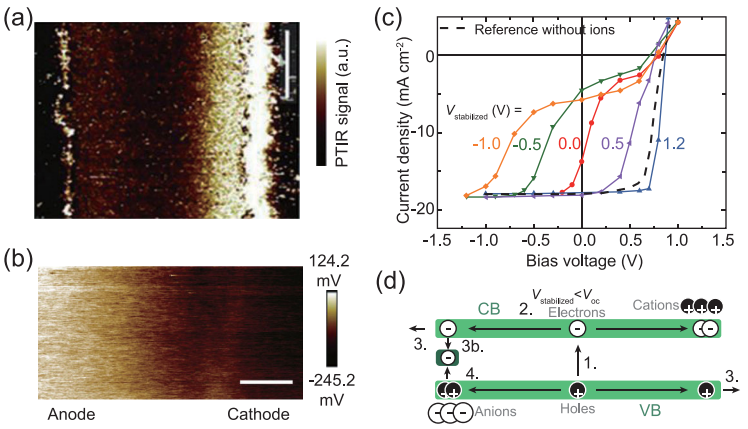

Figure 9. (a) Photothermal induced resonance (PTIR) microscopy of MA^+ group and (b) Kelvin probe contact potential in the perovskite film after electrical poling; (c) simulated current–voltage (*I–V*) curves of the cells with ion migration and interfacial traps; the cell was applied by different steady-state bias voltages before *I–V* measurement; (d) schematic diagram of the ion migration and interfacial traps. Adapted with permission from [101,107].

($V_{stabilized}$) is applied to accumulate different densities of ions at the interface, and at different $V_{stabilized}$, the cells show different *I–V* characteristics in Fig. 9d. In the meantime, considering the ion migration process, time-dependent *I–V* curves are simulated.

The influence of ion migration on the electric properties of the film was also investigated by our lab-made optoelectro-modulated TPV/TPC system (M-TPV/M-TPC), as shown in Fig. 10a [108]. This measurement system can experimentally probe the charge dynamics while modulating the electric field and light illumination, and thus can provide more valuable information on the physical properties, operating mechanisms and device performance of solar cells or other related photoelectric devices [108–109]. A negative electric field was found in the perovskite film close to the TiO_2/perovskite interface when a positive bias voltage was applied. By simulation, this negative electric field can be induced only by additional interfacial doping. This additional interfacial doping derived from ion migration will cause photoelectrical hysteresis, but cannot decrease the open-circuit voltage (V_{oc}). When a constant interfacial trap is also considered, V_{oc} would not be influenced either. Only when both the interfacial doping and trap density are influenced by the ion migration, a negative electric field and V_{oc} will change, thus leading to obvious photoelectric hysteresis, as shown in Fig. 10b–d. It is thus concluded that the ion migration in the perovskite can change both the intrinsic doping and defect properties of the film [109–110]. This will finally influence the electric field and charge dynamic properties of PSCs. However, quantitative relationships between the ion accumulation, the change of doping and defect density have not been established yet.

STABILITY

Although the high PCE of the PSCs exhibited attractive potential for commercial application, its stability issue makes people a little worried as the PSCs in the NREL efficiency chart are labeled with 'not stabilized" [6]. Obviously, the stability issue is the most important problem to be solved at the current point. Therefore, research work on the stability of perovskite solar cells as well as relevant influencing factors has been widely investigated. Humidity, electrical field (including applied bias), UV radiation, thermal treatment and even some additives in the hole-transportation material are generally considered as common extrinsic incentives to the degradation of organic–inorganic perovskite materials and PSCs [111–112].

The humidity degradation mechanism of organic–inorganic perovskite materials is supposed to be that perovskite materials can react with water to hydrate intermediate compounds and finally decompose into PbI_2 [113]. For example, $CH_3NH_3PbI_3$ readily reacts with water to monohydrate $CH_3NH_3PbI_3{\cdot}H_2O$, dihydrate $(CH_3NH_3)_4PbI_6{\cdot}2H_2O$ and eventually decomposes into CH_3NH_3I and PbI_2. An effective method to suppress this degradation is to prevent humidity penetration, i.e. some surface passivation materials including hydrophobic materials have been employed to modify the perovskite film, such as crystal crosslinkers, a non-hydrolytic Al_2O_3 layer, polystyrene and so on [114–116]. PSCs with encapsulation materials (e.g. a Teflon polymer layer, bifunctional polydimethylsiloxane and so on) have also been reported [117–118]. Another method is to use an insulating hygroscopic-like polymer polyethylene glycol (PEG) as the scaffold, which is supposed to work as a moisture absorber around the perovskite crystals, thus restraining the moisture from permeating and reacting with the perovskites [119]. The device based on a hygroscopic PEG scaffold can present an extraordinarily stable behavior at a humidity of 70% for 300 h.

Photo-induced degradation of perovskites is mainly supposed to depend on the hybrid perovskite compositions in the crystal structure, which is also related to the light intensity and the temperature [29,120]. In particular, TiO_2 is a typical photocatalyst for oxidizing water to afford hydroxyl radicals which can oxidize organic materials as well. Therefore, light irradiation containing a small amount

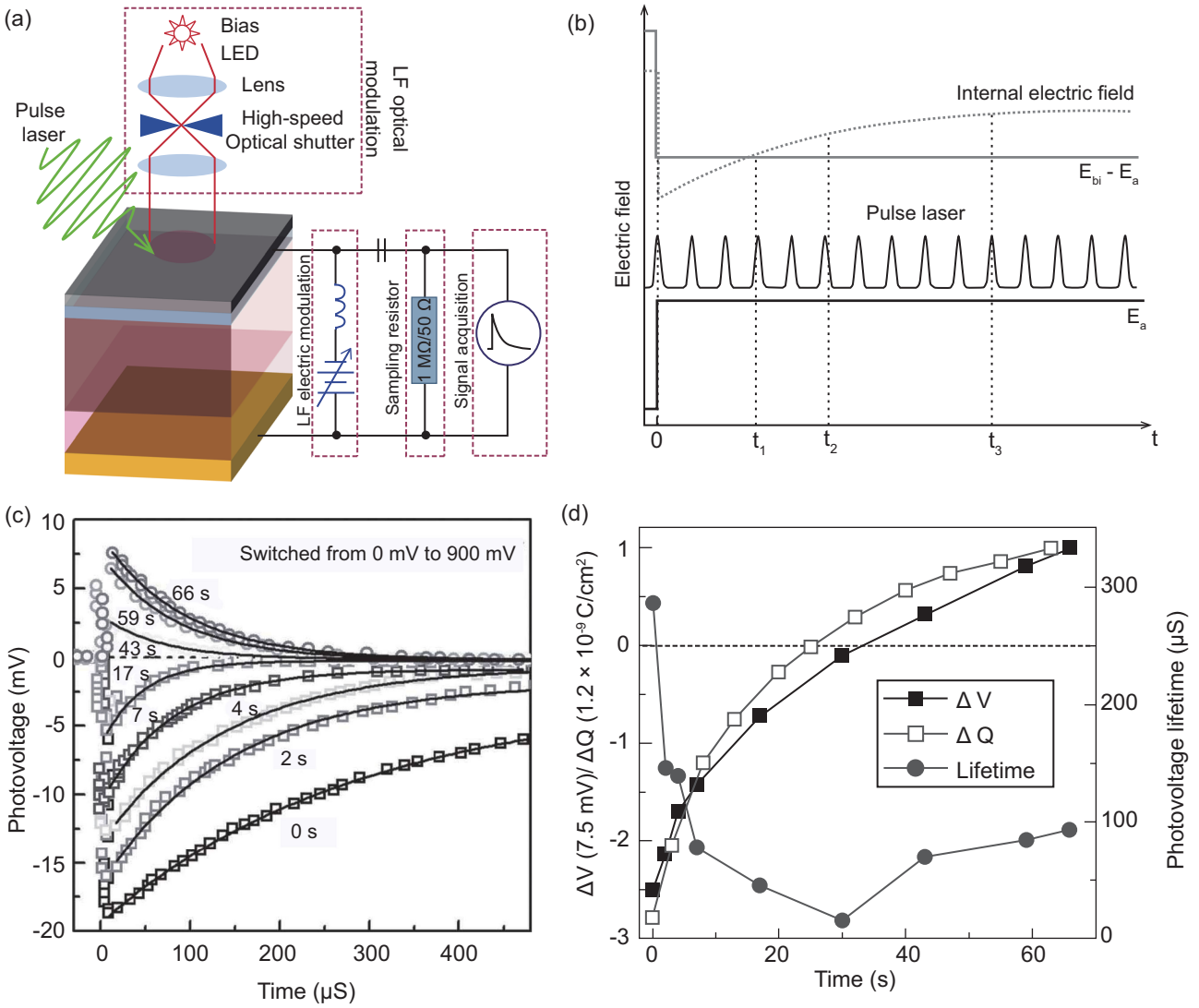

Figure 10. Schematic diagrams of (a) our electrically modulated transient photovoltage/photocurrent measurement system (TPV/TPC); (b) electric field profile across the cell when both the interfacial doping and defect are considered, where E_a is the external modulation and E_{bi} is the junction built-in electric field; (c) transient photovoltage results at different times after the bias voltage at the cell is switched from 0 to 900 mV and (d) the evolution of collected photo-induced charge, peak photovoltage and photovoltage lifetime with time in dark. Adapted with permission from [108–109].

of UV light with the existence of O_2 can degrade the meso-TiO_2-based perovskites film, i.e. the decomposition of iodide-substituted perovskites into HI [121]. Obviously, interfacial modification between mesoporous TiO_2 scaffold and the perovskite, or using other non-UV response electron transport materials, have usually been adopted to improve the photo-induced instability of perovskites [122–123]. Very recently, Shin *et al.* adopted La–$BaSnO_3$ to replace conventional TiO_2, which not only presented a PCE of 21.2% but also retained 93% of its initial performance after 1000 h of full sun illumination [15].

Thermal degradation of organic–inorganic perovskite materials is that the dark-brown perovskite materials gradually turn to yellow PbI_2 with increasing thermal treatment temperature [16]. $CH_3NH_3PbI_3$ was reported to start decomposing at 230°C while its decomposition temperature is 290°C [124]. Of course, the thermal degradation of perovskites is closely related to the moisture and characteristics of perovskite materials [125]. Very recently, with the aid of thermal gravimetric and differential thermal analysis (TG-DTA) coupled with quadrupole mass spectrometry (MS) and first-principles calculations, Juarez-Perez *et al.* found

that the thermal degradation of $MAPbI_3$ and MAI releases methyliodide (CH_3I) and ammonia (NH_3) as degradation products, instead of the common CH_3NH_2 and HI [126]. Furthermore, the key factor to the degradation mechanism is also the instability of the organic cation (i.e. MA^+ or FA^+). Therefore, the most effective way to improve the stability of perovskite is to engineer the compositions of perovskite materials. Mei *et al.* reported $(5\text{-AVA})_x(MA)_{1-x}PbI_3$ perovskite material by partially replacing the MA with 5-aninovaleric (5-AVA) in the cuboctahedral site of typical $MAPbI_3$, and the hole-conductor-free, fully printable mesoporous device based on this material demonstrated excellent long-term stability for more than 1000 h in ambient air under full sunlight illumination [127]. Replacing organic cations with inorganic Cs^+ or Rb^+ is another effective way to stabilize perovskite solar cells [14,16,128]. Besides that, the layered perovskites or named 2D perovskites coupled with carbon electrodes show better resistance to humidity than their 3D analogues [129–130]. Grancini *et al.* reported one-year stable perovskite devices by introducing an ultra-stable 2D/3D $(HOOC(CH_2)_4NH_3)_2PbI_4/CH_3NH_3PbI_3$ perovskite junction, which is an exceptional gradually-organized multidimensional interface, thus presenting a PCE of 12.9% with carbon electrodes and 14.6% with normal mesoporous structure [131].

Very recently, the electric stability issue of PSCs has been gradually recognized. As reported, mobile ions, in particular MA^+ ions, will drift along the electric field and build up certain stress regions within PSCs, leaving ion vacancies [28]. Leijtens *et al.* thought that ion motion alone is reversible and would not degrade PSCs, whereas combining moisture, residual solvent and electric bias may reduce the device stability [132]. In detail, electrical bias can initiate a rapid degradation of perovskite materials under humid conditions. Some investigation further revealed that the existence of grain boundaries will provide fast channels for ion transport, where the degradation usually starts [133–134]. Continuous and alternating ion transport in the perovskite will bring about the material degradation and the decay of the cell performance. The key problem lies in the fact that the solar cell has to work under electric fields and light illumination, and the working condition has to switch between day and night. This will definitely induce irreversible ion migration, and then cause stability issues. Although the mechanism of electrical-field-induced PSC performance deterioration is still under research, seeking suitable ways to suppress the ion migration and reduce the grain boundaries is imperative for improving the stability of PSCs.

SUMMARY AND PROSPECTS

Perovskite materials are already a kind of star material and receive much more attention from the research community, especially in the field of materials science and photovoltaics. So far, perovskite solar cells have already exhibited over 22% efficiency, comparable to CdTe and CIGS solar cells. Perovskite materials are even expected to have the potential to change the current photovoltaics landscape. As we know, the ultimate goal of a photovoltaic technology is to realize its commercialization and wide application. To PSCs, although great progress has been achieved, there is still a long way to go until its practical application in the PV market. To further enhance the cell performance and speed up the commercialization, several issues need to be addressed in the future.

First of all, the stability issue is of primary importance. As inorganic–organic hybrid perovskites and devices are susceptible to environmental factors (i.e. moisture, UV light, oxygen, heating), the instability problems of PSCs under outdoor conditions must be resolved. These degradation pathways can be circumvented by appropriate encapsulation, such as using waterproof, airtight coating and UV-protective coating. In addition, the key instabilities are interfacial and electrical-field-induced instability issues, which are strongly dependent on ion migration in the perovskite itself. This ion migration may be intrinsic and cannot be solved by device encapsulation. Further investigation has revealed that ion migration may be responsible for many unusual phenomena in the perovskite and the devices, such as *I-V* hysteresis, the switchable photovoltaic effect, the giant dielectric constant, photo-induced phase separation, the photo-induced self-poling effect and electrical-field-driven reversible conversion between PbI_2 and perovskite [135]. Therefore, a thorough understanding of the ion migration mechanism is crucial at both experimental and theoretical levels and is expected to help us develop appropriate methodologies to control ion migration in the future. Currently, material engineering and interfacial engineering are generally considered to be effective ways to reduce grain boundaries to prevent ion migration and the decomposition of the perovskite film as well as to improve the stability. Some new methodologies and technologies are also imperative in the future.

Secondly, much more effort is still needed to deeply understand the photophysics of perovskites and the devices. Currently, by various time-resolved spectroscopy techniques and theoretical calculation, some physical properties of perovskite materials have been investigated, which can further confirm their superiority in the charge transfer/separation

characteristics coupled with the suppressed charge recombination, an extremely shallow trap depth (10 meV) with a low trap-state concentration, ultralong diffusion length and so on. For the whole device, however, when the doping, defects and static charge distribution vary inside the perovskite material, the variety of basic dynamic processes is still unclear, especially when the device is operating. From this perspective, in-depth understanding the intrinsic physics of perovskites and devices is the key to further improve the cell performance and the stability issue.

Thirdly, developing large-area stable PSCs and modules is inevitable to realize their commercialization and wide application. Recently, people have attempted realistic ways (especially fabrication techniques) to obtain highly efficient largescale PSCs. The one-step anti-solvent spin-coating method has been proved to be a state-of-the-art technology; however, it is not suitable for largescale devices. Some research groups have developed different perovskite film deposition methods suitable for largescale devices; a certified PCE as high as 19.7% of 1-cm^2-sized PSCs has been achieved [35,69,136]. Grancini *et al.* fabricated 10 × 10 cm^2 solar modules by a fully printable industrial-scale process, presenting a PCE of 11.2% with zero loss in cell performance for over 10 000 h measured under controlled standard conditions [131]. As we know, for a largescale PSC, the defect density, the crystal size, film uniformity and the electron collecting resistances are significant challenges. Therefore, several aspects have to be considered, such as the balance between fabrication technique and cell performance, and the relationship between interface properties and device efficiency, of course, still including the hysteresis and stability.

Fourthly, highly efficient PSCs are based on lead-based perovskites, all of which contain the toxic Pb element. More importantly, halide perovskites can easily dissolve in water, thus leading to more concern about the toxicity issue when largescale application of PSCs will be on the agenda. Obviously, to facilitate the practical application, the toxicity issue of the lead element cannot be ignored; however, how to handle this problem is still under debate. In fact, developing highly efficient, stable lead-free alternatives may permanently solve this issue. Currently, pure Sn-based PSCs struggle to repeat the high performance of Pb-based devices [57,80]. Therefore, further enhancement in cell performance and stability is necessary, which is expected to come from fundamental research on understanding the electron dynamics and interfacial engineering.

Overall, with these mixed halide perovskite materials, higher efficiency is still possible through structural modification along with bandgap tuning. In the meantime, higher V_{oc} is also expected by careful control of the luminescent property of the perovskite, thus leading to higher PCE. Fabricating highly efficient, stable PSCs is a systematic and multidisciplinary project, which requires contributions from semiconductor physicists, organic chemists, material scientists and even engineers. With substantial efforts toward developing hybrid perovskite materials, it is believed that a kind of reliable photovoltaic technology based on perovskites can be realized in the future.

FUNDING

This work was supported by the National Natural Science Foundation of China (91433205, 51627803, 51402348, 51421002, 21173260 and 11474333) and the Knowledge Innovation Program of the Chinese Academy of Sciences.

REFERENCES

1. Green MA, Emery K and Hishikawa Y *et al.* Solar cell efficiency tables (version 48). *Prog Photovolt Res Appl* 2016; **24**: 905–13.
2. Jackson P, Wuerz R and Hariskos D *et al.* Effects of heavy alkali elements in Cu(In, Ga)Se_2 solar cells with efficiencies up to 22.6%. *Phys Status Solidi Rapid Res Lett* 2016; **10**: 583–6.
3. Grätzel M, Mitzi DB and Sargent EH *et al.* Materials interface engineering for solution-processed photovoltaics. *Nature* 2012; **488**: 304–12.
4. Eslamian M. Inorganic and organic solution-processed thin film devices. *Nano-Micro Lett* 2017; **9**: 3.
5. Razza S, Castro-Hermosa S and Brown TM *et al.* Research update: large-area deposition, coating, printing, and processing techniques for the upscaling of perovskite solar cell technology. *APL Mater* 2016; **4**: 091508.
6. National Renewable Energy Laboratory Service. Photovoltaic Research: Efficiency Chart. https://www.nrel.gov/pv/assets/images/efficiency-chart.png (4 September 2017, date last accessed).
7. Cai M, Wu Y and Han L *et al.* Cost-performance analysis of perovskite solar modules. *Adv Sci* 2017; **4**: 1600269.
8. Saparov B and Mitzi DB. Organic-inorganic perovskites: structural versatility for functional materials design. *Chem Rev* 2016; **116**: 4558–96.
9. Kojima A, Teshima K and Miyasaka T *et al.* Organometal halide perovskites as visible-light sensitizers for photovoltaic cells. *J Am Chem Soc* 2009; **131**: 6050–1.
10. Im JH, Lee CR and Park NG *et al.* 6.5% efficient perovskite quantum-dot-sensitized solar cell. *Nanoscale* 2011; **3**: 4088–93.
11. Kim HS, Gratzel M and Park NG *et al.* Lead iodide perovskite sensitized all-solid-state submicron thin film mesoscopic solar cell with efficiency exceeding 9%. *Sci Rep* 2012; **2**: 591.
12. Lee MM, Teuscher J and Snaith HJ *et al.* Efficient hybrid solar cells based on meso-superstructured organometal halide perovskites. *Science* 2012; **338**: 643–7.

13. Burschka J, Pellet N and Grätzel M *et al.* Sequential deposition as a route to high-performance perovskite-sensitized solar cells. *Nature* 2013; **499**: 316–20.
14. Saliba M, Matsui T and Grätzel M *et al.* Cesium-containing triple cation perovskite solar cells: improved stability, reproducibility and high efficiency. *Energy Environ Sci* 2016; **9**: 1989–97.
15. Shin SS, Noh JH and Seok SI *et al.* Colloidally prepared La-doped $BaSnO_3$ electrodes for efficient, photostable perovskite solar cells. *Science* 2017; **356**: 167–71.
16. Saliba M, Matsui T and Grätzel M *et al.* Incorporation of rubidium cations into perovskite solar cells improves photovoltaic performance. *Science* 2016; **354**: 206–9.
17. Tsai H, Nie W and Mohite AD *et al.* High-efficiency two-dimensional Ruddlesden-Popper perovskite solar cells. *Nature* 2016; **536**: 312–7.
18. Green MA, Emery K and Hishikawa Y *et al.* Solar cell efficiency tables (version 49). *Prog Photovolt Res Appl* 2017; **25**: 3–13.
19. Park NG, Grätzel M and Emery K *et al.* Towards stable and commercially available perovskite solar cells. *Nat Energy* 2016; **1**: 16152.
20. Seo J, Noh JH and Seok SI. Rational strategies for efficient perovskite solar cells. *Acc Chem Res* 2016; **49**: 562–72.
21. Meng L, You J and Yang Y *et al.* Recent advances in the inverted planar structure of perovskite solar cells. *Acc Chem Res* 2016; **49**: 155–65.
22. Rong Y, Liu L and Han H *et al.* Beyond efficiency: the challenge of stability in mesoscopic perovskite solar cells. *Adv Energy Mater* 2015; **5**: 1501066.
23. Zhang F, Wang S and Grätzel M *et al.* Isomer-pure bis-PCBM-assisted crystal engineering of perovskite solar cells showing excellent efficiency and stability. *Adv Mater* 2017; **29**: 1606806.
24. Shi J, Xu X and Meng Q *et al.* Interfaces in perovskite solar cells. *Small* 2015; **11**: 2472–86.
25. Manser JS and Kamat PV. Band filling with free charge carriers in organometal halide perovskites. *Nat Photon* 2014; **8**: 737–43.
26. Green MA, Ho-Baillie A and Snaith HJ. The emergence of perovskite solar cells. *Nat Photon* 2014; **8**: 506–14.
27. Baikie T, Fang Y and Kadro JM *et al.* Synthesis and crystal chemistry of the hybrid perovskite $(CH_3NH_3)PbI_3$ for solid-state sensitized solar cell applications. *J Mater Chem A* 2013; **1**: 5628–41.
28. Stranks SD, Eperson GE and Snaith HJ *et al.* Electron-hole diffusion lengths exceeding 1 micrometer in an organometal trihalide perovskite absorber. *Science* 2013; **342**: 341–4.
29. Stoumpos CC, Malliakas CD and Kanatzidis MG. Semiconducting tin and lead iodide perovskites with organic cations: phase transitions, high mobilities, and near-infrared photoluminescent properties. *Inorg Chem* 2013; **52**: 9019–38.
30. Xing G, Mathews N and Sum TC *et al.* Long-range balanced electron-and hole-transport lengths in organic-inorganic $CH_3NH_3PbI_3$. *Science* 2013; **342**: 344–7.
31. Chen Q, Zhou H and Yang Y *et al.* Under the spotlight: The organic-inorganic hybrid halide perovskite for optoelectronic applications. *Nano Today* 2015; **10**: 355–96.
32. Gao P, Grätzel M and Nazeruddin MK. Organohalide lead perovskites for photovoltaic applications. *Energy Environ Sci* 2014; **7**: 2448–63.
33. Xiao M, Cheng YB and Spiccia L *et al.* A fast deposition-crystallization procedure for highly efficient lead iodide perovskite thin-film solar cells. *Angew Chem Int Ed* 2014; **53**: 9898–903.
34. Yin M, Xie F and Han L *et al.* Annealing-free perovskite films by instant crystallization for efficiency solar cells. *J Mater Chem A* 2016; **4**: 8548–53.
35. Li X, Bi DQ and Grätzel M *et al.* A vacuum flash-assisted solution process for high-efficiency large-area perovskite solar cells. *Science* 2016; **353**: 58–62.
36. Xiao J, Yang Y and Meng Q *et al.* Pressure-assisted $CH_3NH_3PbI_3$ morphology reconstruction to improve the high performance of perovskite solar cells. *J Mater Chem A* 2015; **3**: 5289–93.
37. Zhu L, Shi J and Meng Q *et al.* Temperature-assisted controlling morphology and charge transport property for highly efficient perovskite solar cells. *Nano Energy* 2015; **15**: 540–8.
38. Chen Q, Zhou H and Yang Y *et al.* Planar heterojunction perovskite solar cells via vapor assisted solution process. *J Am Chem Soc* 2014; **136**: 622–5.
39. Ono LK, Leyden MR and Qi Y *et al.* Organometal halide perovskite thin films and solar cells by vapor deposition. *J Mater Chem A* 2016; **4**: 6693–713.
40. Yin J, Qu H and Zheng N *et al.* Vapor-assisted crystallization control toward high performance perovskite photovoltaics with over 18% efficiency in the ambient atmosphere. *J Mater Chem A* 2016; **4**: 13203–10.
41. Owoade OK, Salau AM and Akande AR *et al.* Annealing effect on the structural properties of the alloy of $PbCl_2$ and NaCl thin film. *Indian J Pure Appl Phys* 2000; **38**: 499–503.
42. Mitzi DB, Prikas MT and Chondroudis K. Thin film deposition of organic-inorganic hybrid materials using a single source thermal ablation technique. *Chem Mater* 1999; **11**: 542–4.
43. Liu M, Johnston MB and Snaith HJ. Efficient planar heterojunction perovskite solar cells by vapor deposition. *Nature* 2013; **501**: 395–8.
44. Malinkiewicz O, Yella A and Bolink HJ *et al.* Perovskite solar cells employing organic charge-transport layers. *Nat Photon* 2014; **8**: 128–32.
45. Leyden MR, Jiang Y and Qi Y. Chemical vapor deposition grown formamidinium perovskite solar modules with high steady state power and thermal stability. *J Mater Chem A* 2016; **4**: 13125–32.
46. Jeon NJ, Noh JH and Seok SI *et al.* Solvent engineering for high-performance inorganic-organic hybrid perovskite solar cells. *Nat Mater* 2014; **13**: 897–903.
47. Fan R, Huang Y and Zhou H *et al.* The progress of interface design in perovskite-based solar cells. *Adv Energy Mater* 2016; **6**: 1600460.
48. Noh JH, Im SH and Seok SI *et al.* Chemical management for colorful, efficient, and stable inorganic-organic hybrid nanostructured solar cells. *Nano Lett* 2013; **13**: 1764–9.
49. Yang B, Keum J and Xiao K *et al.* Deciphering halogen competition in organometallic halide perovskite growth. *J Am Chem Soc* 2016; **138**: 5028–35.
50. Chen Y, Gao D and Liang Z *et al.* Efficient and reproducible $CH_3NH_3PbI_{3-x}(SCN)_x$ perovskite based planar solar cells. *Chem Commun* 2015; **51**: 11997–9.
51. Sun Y, Peng J and Liang Z *et al.* Triple-cation mixed-halide perovskites: towards efficient, annealing-free and air-stable solar cells enabled by $Pb(SCN)_2$ additive. *Sci Rep* 2017; **7**: 46193.
52. Daub M and Hillebrecht H. Synthesis, single-crystal structure and characterization of $(CH_3NH_3)_2Pb(SCN)_2I_2$. *Angew Chem Int Ed* 2015; **54**: 11016–7.
53. Xiao Z, Mitzi DB and Yan Y *et al.* Photovoltaic properties of two-dimensional $(CH_3NH_3)_2Pb(SCN)_2I_2$ perovskite: A combined experimental and density functional theory study. *J Phys Chem Lett* 2016; **7**: 1213–8.
54. Jiang Q, Rebollar D and Xu T *et al.* Pseudohalide-induced moisture tolerance in perovskite $CH_3NH_3Pb(SCN)_2I$ thin films. *Angew Chem Int Ed* 2015; **54**: 7617–20.
55. Liu J, Shirai Y and Han L *et al.* High-quality mixed-organic-cation perovskites from a phase-pure non-stoichiometric intermediate $(FAI)_{1-x}$-PbI_2 for solar cells. *Adv Mater* 2015; **27**: 4918–23.

56. Jain A, Voznyy O and Sargent EH. High-throughput screening of lead-free perovskite-like materials for optoelectronic applications. *J Phys Chem C* 2017; **121**: 7183–7.
57. Noel NK, Stranks SD and Snaith HJ *et al.* Lead-free organic-inorganic tin halide perovskites for photovoltaic applications. *Energy Environ Sci* 2014; **7**: 3061–8.
58. Toshniwal A and Kheraj V. Development of organic-inorganic tin halide perovskites: a review. *Sol Energ* 2017; **149**: 54–9.
59. Mosconi E, Umari P and Angelis FD. Electronic and optical properties of mixed Sn-Pb organohalide perovskites: a first principles investigation. *J Mater Chem A* 2015; **3**: 9208–15.
60. Hao F, Stoumpos CC and Chang RPH *et al.* Anomalous band gap behavior in mixed Sn and Pb perovskites enables broadening of absorption spectrum in solar cells. *J Am Chem Soc* 2014; **136**: 8094–9.
61. Vigneshwaran M, Ohta T and Hayase S *et al.* Facile synthesis and characterization of sulfur doped low bandgap bismuth based perovskites by soluble precursor route. *Chem Mater* 2016; **28**: 6436–40.
62. Mitzi DB. Organic-inorganic perovskites containing trivalent metal halide layers: the templating influence of the organic cation layer. *Inorg Chem* 2000; **39**: 6107–13.
63. Slavney AH, Hu T and Karunadasa HI *et al.* A bismuth-halide double perovskite with long carrier recombination lifetime for photovoltaic applications. *J Am Chem Soc* 2016; **138**: 2138–41.
64. Shi D, Adinolfi V and Bakr OM *et al.* Low trap-state density and long carrier diffusion in organolead trihalide perovskite single crystals. *Science* 2015; **347**: 519–22.
65. Fu W, Li H and Chen H *et al.* Controlled crystallization of $CH_3NH_3PbI_3$ films for perovskite solar cells by various PbI_2(X) complexes. *Sol Energ Mater Sol Cells* 2016; **155**: 331–40.
66. Jo Y, Oh KS and Kim DS *et al.* High performance of planar perovskite solar cells produced from PbI_2(DMSO) and PbI_2(NMP) complexes by intramolecular exchange. *Adv Mater* 2016; **3**: 1500768.
67. Li L, Wang X and Zhou H *et al.* The additive coordination effect on hybrid perovskite crystallization and high-performance solar cell. *Adv Mater* 2016; **28**: 9862–8.
68. Lee JW, Kim HS and Park NG. Lewis acid-base adduct approach for high efficiency perovskite solar cells. *Acc Chem Res* 2016; **49**: 311–9.
69. Yang WS, Noh JH and Seok SI *et al.* Iodide management in formamidinium-lead-halide-based perovskite layers for efficient solar cells. *Science* 2017; **356**: 1376–9.
70. Liu Z, Chen Q and Zhou H *et al.* Chemical reduction of intrinsic defects in thicker heterojunction planar perovskite solar cells. *Adv Mater* 2016; **29**: 1606774.
71. Yin WJ, Shi T and Yan Y. Unusual defect physics in $CH_3NH_3PbI_3$ perovskite solar cell absorber. *Appl Phys Lett* 2014; **104**: 063903.
72. Shi T, Yin WJ and Yan Y. Predictions for p-type $CH_3NH_3PbI_3$ perovskites. *J Phys Chem C* 2014; **118**: 25350–4.
73. Wang Q, Shao Y and Huang J *et al.* Qualifying composition dependent *p* and *n* self-doping in $CH_3NH_3PbI_3$. *Appl Phys Lett* 2014; **105**: 163508.
74. Shi J, Wei H and Meng Q *et al.* Control of charge transport in the perovskite $CH_3NH_3PbI_3$ thin film. *ChemPhysChem* 2015; **16**: 842–7.
75. Hao P, Stoumpos CC and Kanatzidis MG *et al.* Lead-free solid-state organic-inorganic halide perovskite solar cells. *Nat Photon* 2014; **4**: 489–94.
76. Stoumpos CC and Kanatzidis MG. The renaissance of halide perovskites and their evolution as emerging semiconductors. *Acc Chem Res* 2015; **48**: 2791–802.
77. Oku T, Ohishi Y and Suzuki A. Effects of antimony addition to perovskite-type $CH_3NH_3PbI_3$ photovoltaic devices. *Chem Lett* 2016; **45**: 134–6.
78. Wang ZK, Li M and Yang YG *et al.* High efficiency Pb-In binary perovskite solar cells. *Adv Mater* 2016; **28**: 6695–703.
79. Chen Q, Cai J and Chen L *et al.* Ag-incorporated organic-inorganic perovskite films and planar heterojunction solar cells. *Nano Lett* 2017; **17**: 3231–7.
80. Abdi-Jalebi M, Dar MI and Sadhanala A *et al.* Impact of monovalent cation halide additives on the structural and optoelectronic properties of $CH_3NH_3PbI_3$ perovskite. *Adv Energy Mater* 2016; **6**: 1502472.
81. Sze SM and Kwok KN. *Physics of Semiconductor Devices*, 3rd edn. New York:Wiley, 2006.
82. Shi J, Dong J and Meng Q *et al.* Hole-conductor-free perovskite organic lead iodide heterojunction thin-film solar cells: High efficiency and junction property. *Appl Phys Lett* 2014; **104**: 063901.
83. Bergmann VW, Weber SA and Ramos FJ *et al.* Real-space observation of unbalanced charge distribution inside a perovskite-sensitized solar cell. *Nat Commun* 2014; **5**: 5001.
84. Guerrero A, Juarez-Perez EJ and Bisquert J *et al.* Electrical field profile and doping in planar lead halide perovskite solar cells. *Appl Phys Lett* 2014; **105**: 133902.
85. Jiang CS, Yang M and Zhou Y *et al.* Carrier separation and transport in perovskite solar cells studied by nanometer-scale profiling of electrical potential. *Nat Commun* 2015; **6**: 8397.
86. Laban WA and Etgar L. Depleted hole conductor-free lead halide iodide heterojunction solar cells. *Energy Environ Sci* 2013; **6**: 3249–53.
87. Bi C, Shao Y and Huang J *et al.* Understanding the formation and evolution of interdiffusion grown organolead halide perovskite thin films by thermal annealing. *J Mater Chem A* 2014; **2**: 18508–14.
88. Shi J, Luo Y and Meng Q *et al.* Modified two-step deposition method for high-efficiency $TiO_2/CH_3NH_3PbI_3$ heterojunction solar cells. *ACS Appl Mater Interfaces* 2014; **6**: 9711–8.
89. Samiee M, Konduri S and Ganapathy B *et al.* Defect density and dielectric constant in perovskite solar cells. *Appl Phys Lett* 2014; **105**: 153502.
90. Baumann A, Väth S and Dyakonov V *et al.* Identification of trap states in perovskite solar cells. *J Phys Chem Lett* 2015; **6**: 2350–4.
91. Chen H, Jen AKY and Chen H *et al.* Molecular engineering hole-extraction materials to enable dopant-free, efficient p-i-n perovskite solar cells. *Adv Energy Mater* 2017; **7**: 1700012.
92. Xiao Z, Dong Q and Huang J *et al.* Solvent annealing of perovskite-induced crystal growth for photovoltaic-device efficiency enhancement. *Adv Mater* 2014; **26**: 6503–9.
93. Heo JH, Song DH and Im SH *et al.* Planar $CH_3NH_3PbI_3$ perovskite solar cells with constant 17.2% average power conversion efficiency irrespective of the scan rate. *Adv Mater* 2015; **27**: 3424–30.
94. Shao Y, Xiao Z and Huang J *et al.* Origin and elimination of photocurrent hysteresis by fullerene passivation in $CH_3NH_3PbI_3$ planar heterojunction solar cells. *Nat Commun* 2014; **5**: 5784.
95. Stranks SD, Burlakov VM and Snaith HJ *et al.* Recombination kinetics in organic-inorganic perovskites: excitons, free charge, and subgap states. *Phys Rev Appl* 2014; **2**: 034007.
96. Noel NK, Abate A and Snaith HJ *et al.* Enhanced photoluminescence and solar cell performance via Lewis based passivation of organic-inorganic lead halide perovskites. ACS Nano 2014; **8**: 9815–21.
97. Yang D, Yang R and Liu S *et al.* Hysteresis-suppressed high-efficiency flexible perovskite solar cells using solid-state ionic-liquid for effective electron transport. *Adv Mater* 2016; **28**: 5206–13.

98. Liu Y, Zhang Y and Liu S *et al*. Thinness- and shape-controlled growth for ultrathin single-crystalline perovskite wafers for mass production of superior photoelectronic devices. *Adv Mater* 2016; **28**: 9204–9.
99. Baldini A and Bruzzi M. Thermally stimulated current spectroscopy: Experimental techniques for the investigation of silicon detectors. *Rev Sci Instrum* 1993; **64**: 932–6.
100. Micocci G, Rizzo A and Tepore A. Trapping center parameters in indium selenide single crystals by thermally stimulated current measurements. *J Appl Phys* 1983; **564**: 1924–9.
101. Yuan Y, Chae J and Huang J *et al*. Photovoltaic switching mechanism in lateral structure-hybrid perovskite solar cells. *Adv Energy Mater* 2015; **5**: 1500615.
102. deQuilettes DW, Zhang W and Strank SD *et al*. Photo-induced halide redistribution in organic-inorganic perovskite films. *Nat Commun* 2016; **7**: 11683.
103. Deng Y, Xiao Z and Huang J. Light-induced self-poling effect on organometal trihalide perovskite solar cells for increased device efficiency and stability. *Adv Energy Mater* 2015; **5**: 1500721.
104. Yuan Y and Huang J. Ion migration in organometal trihalide perovskite and its impact on photovoltaic efficiency and stability. *Acc Chem Res* 2016; **49**: 286–93.
105. Xiao Z, Yuan Y and Huang J *et al*. Giant switchable photovoltaic effect in organometal trihalide perovskite devices. *Nat Mater* 2015; **14**: 193–8.
106. Eames C, Frost JM and Islam MS *et al*. Ionic transport in hybrid lead iodide perovskite solar cells. *Nat Commun* 2015; **6**: 7497.
107. Reenen SV, Kemerink M and Snaith HJ, Modeling anomalous hysteresis in perovskite solar cells. *J Phys Chem Lett* 2015; **6**: 3808–14.
108. Shi J, Li D and Meng Q *et al*. Opto-electro-modulated transient photovoltage and photocurrent system for investigation of charge transport and recombination in solar cells. *Rev Sci Instrum* 2016; **87**: 123107.
109. Shi J, Zhang H and Meng Q *et al*. Microscopic charge transport and recombination processes behind the photoelectric hysteresis in perovskite solar cells. *Small* 2016; **32**: 5288–94.
110. Shi J, Xu X and Meng Q *et al*. Intrinsic slow charge response in the perovskite solar cells: Electron and ion transport. *Appl Phys Lett* 2015; **107**: 163901.
111. Wang D, Wright M and Elumalai NK *et al*. Stability of perovskite solar cells. *Sol Energ Mater Sol Cells* 2016; **147**: 255–75.
112. Yue Y, Salim NT and Han L *et al*. Enhanced stability of perovskite solar cells through corrosion-free pyridine derivatives in hole-transporting materials. *Adv Mater* 2016; **28**: 10738–43.
113. Frost JM, Butler KT and Walsh A *et al*. Atomistic origins of high-performance in hybrid halide perovskite solar cells. *Nano Lett* 2014; **14**: 2584–90.
114. Wang Q, Dong Q and Huang J *et al*. Thin insulating tunneling contacts for efficient and water-resistant perovskite solar cells. *Adv Mater* 2016; **28**: 6734–9.
115. Zhao Y, Yu D and Zhao Q *et al*. A polymer scaffold for self-healing perovskite solar cells. *Nat Commun* 2015; **7**: 1038.
116. Yue Y, Yang X and Han L *et al*. Selective deposition of insulating metal oxide in perovskite solar cells with enhanced device performance. *ChemSusChem* 2015; **8**: 2625–9.
117. Kim IS and Martinson ABF. Stabilizing hybrid perovskites against moisture and temperature *via* non-hydrolytic atomic layer deposited overlayers. *J Mater Chem A* 2015; **3**: 20092–6.
118. Li X, Dar MI and Grätzel M *et al*. Improved performance and stability of perovskite solar cells by crystal crosslinking with alkylphosphonic acid ω;-ammonium chlorides. *Nat Chem* 2015; **7**: 703–11.
119. Zhao Y, Wei J and Yu D et *al*. A polymer scaffold for self-healing perovskite solar cells. *Nat Commun* 2016; **7**: 10228.
120. Leijtens T, Hoke ET and Snaith HJ *et al*. Stability of metal halide perovskite solar cells. *Adv Energy Mater* 2015; **5**: 1500963.
121. Ito S, Tanaka S and Manabe K *et al*. Effects of surface blocking layer of Sb_2S_3 on nanocrystalline TiO_2 for $CH_3NH_3PbI_3$ perovskite solar cells. *J Phys Chem C* 2014; **118**: 16995–7000.
122. Li W, Li J and Wang L *et al*. Effect of cesium chloride modification on the film morphology and UV-induced stability of planar perovskite solar cells. *J Mater Chem A* 2016; **4**: 11688–95.
123. Li W, Zhang W and Snaith HJ *et al*. Enhanced UV-light stability of planar heterojunction perovskite solar cells with caesium bromide interface modification. *Energy Environ Sci* 2016; **9**: 490–8.
124. Dualeh A, Gao P and Grätzel M *et al*. Thermal behavior of methylammonium lead-trihalide perovskite photovoltaic light harvesters. *Chem Mater* 2014; **26**: 6160–4.
125. Misra RK, Aharon S and Katz EA *et al*. Temperature- and component-dependent degradation of perovskite photovoltaic materials under concentrated sunlight. *J Phys Chem Lett* 2015; **6**: 326–30.
126. Juarez-Perez EJ, Hawash Z and Qi Y *et al*. Thermal degradation of $CH_3NH_3PbI_3$ perovskite into NH_3 and CH_3I gases observed by coupled thermogravimetry-mass spectrometry analyses. *Energy Environ Sci* 2016; **9**: 3406–10.
127. Mei A, Li X and Han H *et al*. A hole-conductor-free, fully printable mesoscopic perovskite solar cell with high stability. *Science* 2014; **345**: 295–8.
128. Li Z, Yang M and Zhu K *et al*. Stabilizing perovskite structures by tuning tolerance factor: formation of formamidinium and cesium lead iodide solid-state alloys. *Chem Mater* 2016; **28**: 284–92.
129. Dou L, Wong AB and Yang P *et al*. Atomically thin two-dimensional organic-inorganic hybrid perovskites. *Science* 2015; **349**: 1518–21.
130. Smith IC, Hoke ET and Karunadasa HI *et al*. A layered hybrid perovskite solar-cell absorber with enhanced moisture stability. *Angew Chem Int Ed* 2014; **53**: 11232–5.
131. Grancini G, Roldán-Carmona C and Nazeeruddin MK *et al*. One-year stable perovskite solar cells by 2D/3D interface engineering. *Nat Commun* 2017; **8**: 15684.
132. Leijtens T, Hoke ET and Petrozza A *et al*. Mapping electric field-induced switchable poling and structural degradation in hybrid lead halide perovskite thin films. *Adv Energy Mater* 2015; **5**: 1500962.
133. Yun JS, Seidel J and Seok SI *et al*. Critical role of grain boundaries for ion migration in formamidium and methylammonium lead halide perovksite solar cells. *Adv Energy Mater* 2016; **6**: 1600330.
134. Shao Y, Fang Y and Huang J *et al*. Grain boundary dominated ion migration in polycrystalline organic-inorganic halide perovskite films. *Energy Environ Sci* 2016; **9**: 1752–9.
135. Xing J, Wang Q and Huang J *et al*.. Ultrafast ion migration in hybrid perovskite polycrystalline thin films under light and suppression in single crystals. *Phys Chem Chem Phys* 2016; **18**: 30184–90.
136. Wu Y, Yang X and Han L *et al*. Perovskite solar cells with 18.21% efficiency and area over 1 cm^2 fabricated by heterojunction engineering. *Nat Energy* 2016; **1**: 16148.